CHEMISTRY OF MATERIALS
Cite This: Chem. Mater. 2019, 31, 9040−9048
Article
pubs.acs.org/cm

Bioinspired Synthesis of Quasi-Two-Dimensional Monocrystalline Oxides

Yizhan Wang, Yeqi Shi, Ziyi Zhang, Corey Carlos, Chenyu Zhang, Karishma Bhawnani, Jun Li, Jingyu Wang, Paul M. Voyles, Izabela Szlufarska, and Xudong Wang*

Department of Materials Science and Engineering, University of Wisconsin-Madison, Madison, Wisconsin 53706, United States

Supporting Information

ABSTRACT: Controllable synthesis of two-dimensional (2D) monocrystalline oxide nanomaterials beyond van der Waals solids is intriguing but very challenging. Inspired by the biomineralization processes that commonly implement organic templates with both positive and negative charges for regulating the crystal nucleation and growth, we adapted mix-charges amphiphilic monolayer to the ionic layer epitaxy and enabled the growth of monocrystalline 2D nanosheets. In situ grazing incidence X-ray diffraction and ex situ crystal and elemental analyses revealed that mixing charge in the template is able to tune the 2D crystal nucleation rate and promote the growth of monocrystalline domains. Molecular dynamics simulations suggested that mixing charges could yield a stable, flatter, and more ordered monolayer template with a nonuniform distribution of charges, which are favorable for the growth of monocrystalline nanosheets. Designing the mixed amphiphilic monolayers resulted in the creation of ultrathin nanosheets from various oxides including CoO, Bi_2O_3, MnO_2, and Fe_3O_4 as well as doped ones, opening up an opportunity to broaden the 2D nanomaterial family to functional oxides.

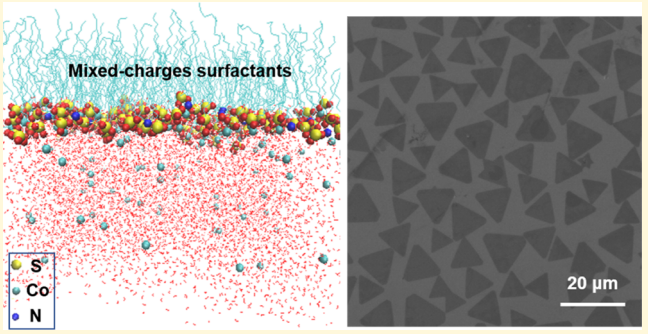

INTRODUCTION

Two-dimensional (2D) nanomaterials are now playing a key role in material innovation and property advancement.[1−4] The family of 2D nanomaterials has rapidly expanded from graphene to transition-metal dichalcogenides, Xenes, black phosphorus, and their heterostructures. However, creating 2D nanomaterials from nonlayered functional materials such as oxides and nitrides still remains a grand challenge for material synthesis, which typically requires stabilization of crystal phases or structures far away from equilibrium.[5−9] A few synthesis strategies have been developed using self-assembled amphiphilic molecules as templates to direct 2D anisotropic growth of nonlayered materials.[9,10] Ionic layer epitaxy (ILE) is a typical example that relies on the ionized head groups in an amphiphilic monolayer to establish an electrical double layer to self-confine the crystal growth within a 2D nanometer regime.[10,11] Nevertheless, the self-assembled templates are always associated with irregular morphology[12,13] and polycrystallinity.[14−16] Understanding of the 2D crystal evolution kinetics is still missing. Therefore, well-defined amphiphilic templates that offer robust control of the crystallinity and 2D morphology from a broad range of materials, beyond those bonded by van der Waals interactions, are critically needed for both synthesis and kinetics studies.

In fact, the amphiphilic-templated crystallization such as ILE is to a large extent similar to biomineralization, a fundamental life process that can be commonly found in living beings to form inorganic crystals through out-of-equilibrium dynamic self-assembly.[17] In this process, the self-assembled organic template offers synergistic effects[18−22] for regulating the aggregation of ions: it directs the nucleation and growth of inorganic crystals and it defines the properties of the resulting structures. For example, in nacre, layers of organic matrix assembled from chitin and proteins control the formation of hexagonal aragonite platelets to achieve complex hierarchical architectures with superb fracture toughness (Figure 1a).[23] The natural presence of both negatively and positively charged amino acid residues (e.g., negative aspartate and glutamate, positive lysine and arginine) in the protein assemblies plays a key role in controlling the growth of aragonite.[18,24−26] Appropriate distribution and conformation of charged groups within proteins assemblies could stabilize nonequilibrium distribution of ionic species[18,27] and lower the nucleation energy barrier for inorganic crystals by offering more accessible binding sites.[19,28−30] Understanding and utilization of mixed charges in the biomineralization templates may exert unprecedented controllability in synthetic material science.[31]

Inspired by the protein-based templates in biomineralization, in this work, we adopted mixed surfactants with positive and negative head groups to direct the ILE synthesis of 2D nanosheets. An appropriate mixing ratio of the opposite surface charges could effectively control the nucleation and crystal-

Received: August 15, 2019
Revised: October 10, 2019
Published: October 11, 2019

DOI: 10.1021/acs.chemmater.9b03307
Chem. Mater. 2019, 31, 9040−9048

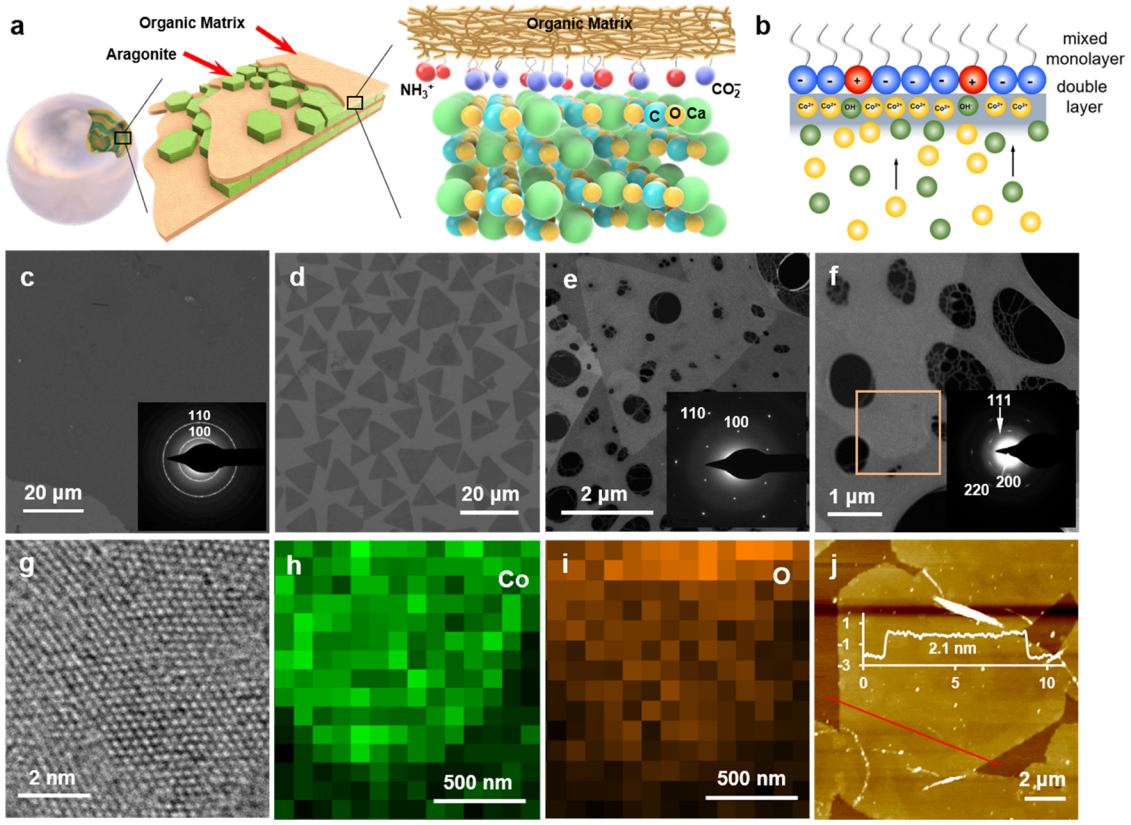

Figure 1. Nanosheet synthesis under mixed surfactants with opposite charges. (a) Layered structure of hexagonal aragonite platelets alternating with the organic matrix in the nacreous layer of pearl and the schematic representation of the protein surface structure with well-mixed positively (red) and negatively (blue) charged amino acid residues directing the biomineralization of aragonite. (b) Schematic illustration of the formation of monocrystalline nanosheets with the mixed monolayer bared positive (red) and negative (blue) charges on the interface of the precursor solution and air. (c) SEM image of the continuous film of $Co(OH)_2$ synthesized with mono SOS as transferred to a SiO_2/Si substrate surface. The inset is the selected area electron diffraction (SAED) pattern of the synthesized film, which indicated the polycrystallinity of the film. (d) SEM image of a triangular $Co(OH)_2$ nanosheet synthesized with a mixed monolayer (SOS/OAM = 9:1) as transferred to a SiO_2/Si substrate surface. (e) Low-magnification TEM image and the selected area electron diffraction (SAED) pattern (inset) of the triangular nanosheet rest on a holy carbon TEM grid. (f) Triangular nanosheets after 10 min of O_2 plasma treatment. The inset is the SAED pattern, which matches well with the CoO structure. (g) High-resolution TEM image showing the crystal lattice of CoO after plasma treatment of the triangular nanosheets. Elemental mapping of (h) cobalt and (i) oxygen in the area of triangular nanosheets marked by the orange box in (f). (j) Topography atomic force microscopy (AFM) image showing the nanometer thickness and good surface flatness of the nanosheets. The inset is the height profile along the red line revealing that the thickness is 2.1 nm.

linity and enabled the formation of large-sized monocrystal nanosheets. This strategy resulted in the formation of ultrathin monocrystalline nanosheets from a range of oxides including CoO, Bi_2O_3, and MnO_2 as well as doped ones, which may become a general synthetic approach for creating 2D nanomaterials from the family of functional oxides.

RESULTS AND DISCUSSION

The schematic ILE synthesis of cobalt hydroxide nanosheets is shown in Figure 1b (synthesis details are in the Experimental Section). In the growth process, mixed anionic oleylsulfate (SOS) and oleylamine (OAM) surfactants self-assembled into a mixed monolayer with excess negative charges at the water–air interface. Positively charged metal ions Co^{2+} were attracted to the interface, forming an ultrathin Co^{2+}-concentrated Stern layer underneath the surfactant monolayer. At an elevated temperature of 60 °C, hexamethylenetetramine (HMTA) decomposed into HCHO and ammonium hydroxide, increasing the pH of the solution and initializing the hydrolysis of Co^{2+}. Nanosheets, thus, were nucleated and grown within the confined 2D region. It was found that the surfactant mixing ratio has a significant influence on the nanosheet morphology. The monosurfactant SOS only produced a continuous film at the water–air interface (Figures 1c and S1a), as in most previous ILE growth of oxides.[15,16] The polycrystalline structure was confirmed by selected area electron diffraction (SAED) ring patterns collected from the nanosheets (the inset of Figure 1c). After mixing with a small amount of OAM (SOS/OAM = 39:1 or 19:1), pores started to evolve in the continuous film (Figure S1b,c). When the mole ratio of SOS/OAM reached 9:1, there appeared a single layer of triangular nanosheets covering the entire water–air interface (Figures 1d and S1d). Further reducing the amount of SOS to a ratio of 7:3 decreased the yield of triangular nanosheets. When the net charge of the monolayer became neutral or positive (SOS/OAM ≤ 5:5), no nanosheets could be formed (Figure S1f–h).

The as-synthesized nanosheets with mixed surfactant (SOS/OAM = 9:1) were transferred onto a SiO_2-coated Si substrate surface where they became visible under the optical microscope (Figure S2). As shown in Figure 1d, the as-transferred nanosheets were densely packed without any overlapping and covered nearly the entire surface (Figure S2). All of the

DOI: 10.1021/acs.chemmater.9b03307
Chem. Mater. 2019, 31, 9040–9048

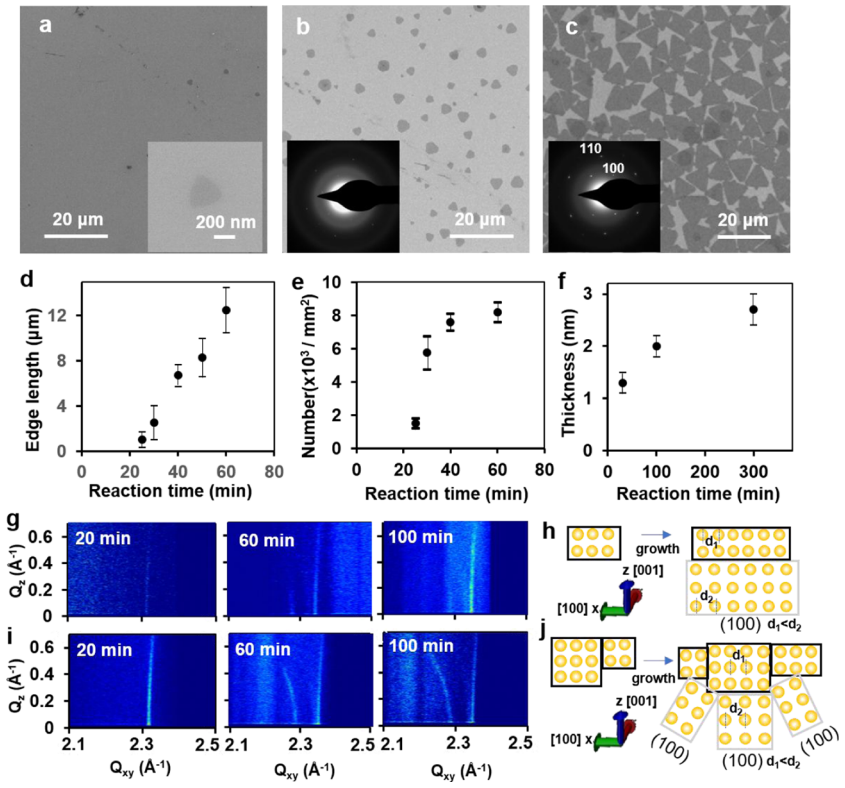

Figure 2. Growth process of a single-crystal triangular nanosheet of $Co(OH)_2$ under mixed monolayers. (a–c) SEM images of triangular nanosheets transferred from the air–water interface with the mixed monolayer (SOS/OAM = 9:1) at different reaction times of 25, 30, 60 min, respectively. The inset of (a) is the enlarged image of the nanosheets; insets in (b, c) are the corresponding SAED pattern of the triangular nanosheets. (d) The average edge length of triangular nanosheets at different reaction time. (e) The average number of triangular nanosheets per millimeter square at different reaction time. (f) The thickness of the triangular nanosheets at different reaction time. (g) Grazing incidence X-ray diffraction (GID) data collected for in situ single-crystal triangular nanosheet growth under the mixed monolayer (SOS/OAM = 9:1) at the different reaction time of 20, 60, and 100 min. (h) Schematic illustration of the nanosheet crystal evolution under the guide of mixed surfactant. (i) GID data collected for in situ polycrystalline film growth under the monolayer of mono SOS at the different reaction time of 20, 60, and 100 min. (j) Schematic illustration of the nanosheet crystal evolution under the guide of mono SOS.

nanosheets appeared to be triangular with edges of 13.0 ± 2.0 μm.

The crystal structure of the nanosheets was characterized by transmission electron microscopy (TEM). The as-prepared ultrathin nanosheets retained their original shape after being transferred to the holey carbon TEM grid (Figure 1e). SAED pattern collected from the nanosheets showed a clear monocrystalline feature with perfect hexagonally arranged diffraction spots (the inset of Figure 1e), which could be indexed to the (110) and (100) facets of β-$Co(OH)_2$, matching well to the fast Fourier transform pattern (Figure S2). The single-crystal $Co(OH)_2$ nanosheets could be directly transformed to CoO by O_2 plasma treatment without changing the triangle morphology (Figure 1f). As shown in the inset of Figure 1f, after 10 min of plasma irradiation, new sets of SAED pattern were obtained, which could be indexed to the (111), (200), and (220) facets of CoO (JCPDS No. 43-1004). High-resolution TEM (HRTEM) image showed that the (200) d-spacing measured to be 0.21 nm (Figure 1g). Local misalignment and dislocations could be observed. Energy-dispersive X-ray spectroscopy (EDS) mapping in the corner area marked by the orange box in Figure 1e showed a uniform distribution of oxygen and cobalt elements in the nanosheet (Figure 1h,i). The atomic ratio between Co and O was confirmed to be ~1:1 by electron energy loss spectroscopy (Figure S3), suggesting a good stoichiometry of the CoO compound.

Atomic force microscopy (AFM) was used to characterize the surface flatness and thickness (Figure 1j). All of the nanosheets exhibited a uniform thickness of 2.1 nm (the inset of Figure 1j). The surface of all nanosheets was generally very flat with a roughness average of R_a = 0.11 nm. X-ray photoelectron spectroscopy (XPS) was employed to confirm the chemical composition and bonding in nanosheets. The full XPS survey spectra from the as-transferred pristine nanosheets on a Si substrate clearly showed the presence of Co, O, and C peaks (Figure S4), where the C signal was from the surfactant monolayer. The surfactant residues could be removed by oxygen plasma. The largely reduced C signal from plasma-treated samples confirmed the successful removal of surfactant residues (Figure S4). The resolved Co 2p peak scans showed that in pristine nanosheets, the Co atoms were bonded with the OH group. After plasma treatment, the main peak of the Co $2p_{3/2}$ and Co $2p_{1/2}$ shifted from 781.6 to 780.6 eV and from 797.1 to 796.2 eV, respectively, which could be attributed to the formation of the Co–O bonds[32] and suggested that the nanosheets were transferred into CoO (Figure S5).

The above findings confirmed the essential role of mixing surfactant charges in synthesizing monocrystalline nanosheets. Just like the biomineralization processes, both the positive and

DOI: 10.1021/acs.chemmater.9b03307
Chem. Mater. 2019, 31, 9040–9048

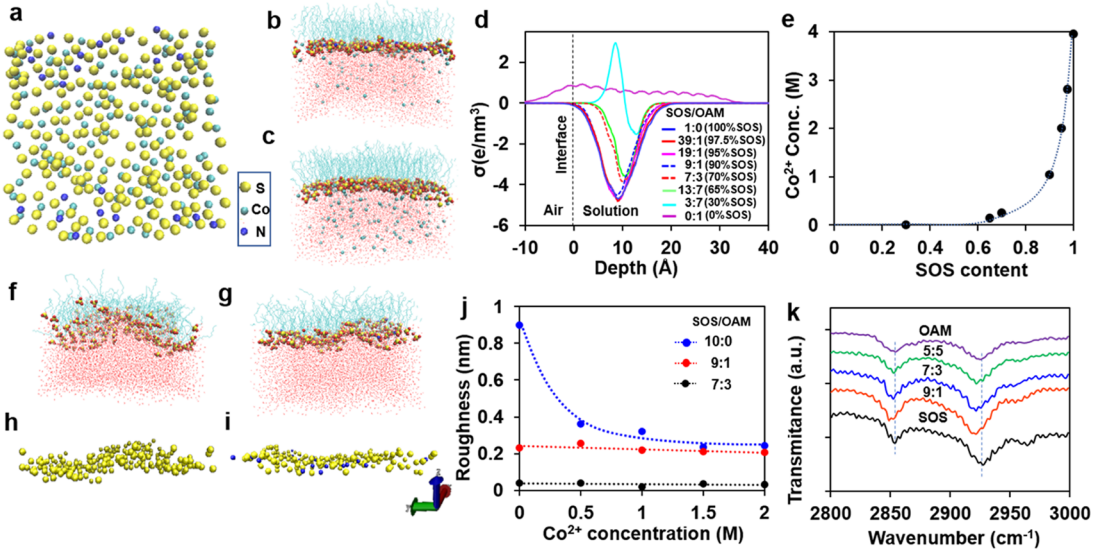

Figure 3. Calculated morphology of the mixed monolayer at the water−vacuum interface. (a) MD simulation-generated surfactant distribution of the mixed monolayer of SOS (S) and OAM (N) (SOS/OAM = 9:1) at the water/vacuum interface with 5 mM Co^{2+} in water. (b) Co^{2+} distribution under the mixed monolayer of SOS and OAM at the ratio of SOS/OAM = 9:1. (c) Co^{2+} distribution under the monolayer of SOS. (d) Charge density as a function of distance from the interface. (e) Calculated average Co^{2+} concentration within a 4 nm thick region below the monolayer for different SOS/OAM ratios (the concentration of Co^{2+} in the bulk solution is 5 mM). (f, g) Simulated monolayer morphology at the interface for mono SOS (f) and SOS/OAM = 9:1 (g). (h, i) The morphology of the monolayer headgroup with 0.5 M Co^{2+} in the adjacent solution for mono SOS (h) and SOS/OAM = 9:1 (i). (j) Roughness of monolayers as a function of Co^{2+} concentration in the adjacent solution for SOS (blue), SOS/OAM = 9:1 (red), and SOS/OAM = 7:3 (black). (k) IR spectra of the mixed monolayer with Co^{2+}.

negative functional groups need to be involved in the templated crystal growth to facilitate crystallization.

To understand the crystallization process under mixed surfactants, nanosheets were collected at different reaction times from the water−air interface. As shown in Figure 2a−c, the triangle nanosheets started to form at ∼25 min. The SAED pattern confirmed their monocrystallinity (the inset of Figure 2b). Before that, there was an incubation period when no crystallites could be observed at the interface (Figure S6). As the reaction time progressed, both the number and the size of nanosheets increased monotonically. Statistical analyses of the nanosheet size distribution revealed a linear relationship between the side length and the reaction time, which increased from 1.0 ± 0.7 μm at 25 min to 12.5 ± 2.0 μm at 60 min (Figure 2d). In contrast, there was an initial sharp jump in the number of the nanosheets, followed by a slow rise during the remaining growth time (Figure 2e). A small increase of the nanosheet thickness (from 1.3 nm at 30 min to 2.7 nm at 300 min) was also observed from the topography AFM measurements (Figures 2f and S7). The time-dependent morphological analyses suggested that the nanosheet nucleation and growth under mix-charge surfactant were similar to the classic LaMer model,[33] where the nucleation of nanosheets was driven by the supersaturation of precursor within the 2D confined ionic layer, followed by the primary lateral growth of individual nuclei. This mechanism is strikingly different from that occurring in the single surfactant system. When only SOS surfactants were used, irregular nuclei nanostructures were formed after a relatively shorter incubation period (Figure S6). These initial nuclei connected to each other form a network, which further grew into a continuous film. It could be seen that the single surfactant monolayer induced a much faster nucleation rate (Figure S6), which resulted in a more irregular growth behavior. Thus, nanocrystalline films with larger roughness were typically obtained.

The evolution of 2D crystals under different surfactant monolayers was further analyzed in situ using grazing incidence X-ray diffraction (GID) (Figure 2g−j). For a mixed SOS/OAM monolayer (SOS/OAM = 9:1), no peaks were observed in the incubation period. After 20 min, a weak and long diffraction rod appeared at Q_{xy} = 2.312 $Å^{-1}$, which indicated the formation of 2D nuclei (Figure 2g). The d value of this peak (2.72 Å) was close to the (100) d-spacing of β-$Co(OH)_2$ (2.75 Å), which ruled out the possibility of contribution from other facets of β-$Co(OH)_2$ (Figure S8). The small shift of the d value was probably due to the strain from the interface (i.e., interacting with the surfactant monolayer). This long diffraction rod became bright and sharp as the reaction time progressed (Figure S9), suggesting that more and larger 2D nanosheets with the same crystal structure have formed. As the reaction time further increased, a short diffraction rod at Q_{xy} = 2.285 $Å^{-1}$ (d = 2.75 Å) with the same d-spacing as the (100) plane of β-$Co(OH)_2$ was observed, suggesting that the crystal lattice was relaxed as the 2D β-$Co(OH)_2$ grew thicker (Figure 2h). The presence of straight and sharp diffraction rods confirmed that all nanosheets were 2D monocrystals with their (001) planes oriented parallel to the water surface. Under mono SOS monolayer, the same long diffraction rod at Q_{xy} = 2.312 $Å^{-1}$ was also observed at 20 min, suggesting the formation of 2D nuclei (Figure 2i). However, in the case of pure SOS, the intensity of the rod was much stronger than for the mixed monolayer at the same reaction time (Figures 2i and S9), which indicated the fast formation of many more nuclei. After 60 min of reaction, a diffraction ring at Q_{xy} = 2.285 $Å^{-1}$ (Q_z = 0) appeared instead of the short straight rod. It was a clear sign that the system became polycrystalline and that the crystallite (001) planes were oriented randomly with respect to the water surface (Figure 2j).

To reveal why the mix-charge surfactants could facilitate the 2D nanosheet growth, molecular dynamics (MD) simulations

DOI: 10.1021/acs.chemmater.9b03307
Chem. Mater. 2019, 31, 9040−9048

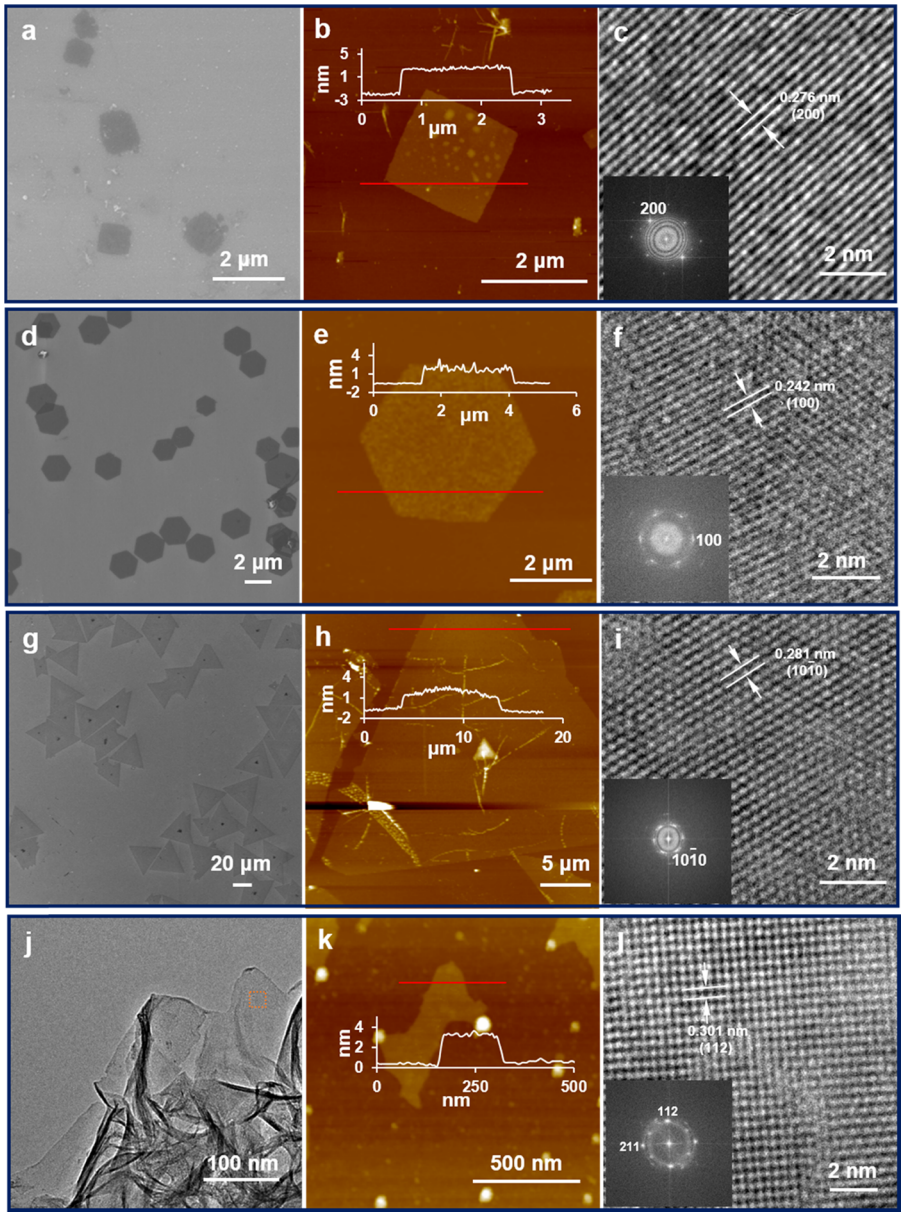

Figure 4. Morphology of single-crystal 2D nanosheets synthesized with mixed monolayers. SEM images (a, d, g), AFM topography images (b, e, h, k), TEM image (j), and high-resolution TEM images (c, f, i, l) of ultrathin 2D nanosheets for Bi_2O_3 (a–c), MnO_2 (d–f), Ni-doped ZnO (g–i), and Fe_3O_4 (j–l). The thickness profiles and SAED patterns of the four metal oxides are shown as the insets in (b, e, h, k, c, f, i, l).

were performed to model the mixed monolayer at the water/vacuum interface and its interaction with Co^{2+} in water (calculation details in the Supporting Information). As shown in Figure 3a, in an equilibrated monolayer, the positively charged OAM was agglomerated into small regions within the negatively charged SOS matrix, forming OAM-rich and OAM-poor regions. At the OAM-rich regions, the Co^{2+} concentration underneath was significantly lower compared to the OAM-poor regions (Figure 3a,b). The regions low in Co^{2+} concentration could form boundaries that confine and isolate nucleation of nanosheets into small zones and, thus, prevent agglomeration at the nucleation stage. In contrast, homogeneous Co^{2+} distribution could be observed under mono SOS surfactant (Figure 3c) and, thus, was more likely to yield a continuous polycrystalline film. Figure 3d compares the charge density distribution near the interface when SOS and OAM were mixed at different ratios. The charge density peaked at ~1 nm below the water/vacuum interface. The interface became less negatively charged as the amount of SOS/OAM ratio decreased and eventually turned to positive when the SOS concentration became lower than 50% (in Figure 3d, we show that results for SOS concentrations of 65 and 30% to be consistent with experiments). The negatively charged surfactant monolayer is expected to induce the formation of a Co^{2+}-concentrated zone underneath and lead to ILE of nanosheets. The simulations reported in Figure 3d were performed for the same Co^{2+} concentration (3 M). However, ion concentration should vary with different SOS/OAM ratios because the ability of the monolayer to attract ion changes. The average Co^{2+} concentration within a 4 nm thick region below the monolayer for different SOS/OAM ratios was calculated from the theory[34] and plotted in Figure 3e. Higher Co^{2+} concentration was obtained for higher SOS/OAM ratios. The Co^{2+} concentration yielded from 9:1 ratio (~1 M) should

DOI: 10.1021/acs.chemmater.9b03307
Chem. Mater. 2019, 31, 9040–9048

be large enough to achieve the appropriate nucleation rate for monocrystalline nanosheet formation, as suggested by the experiment (Figure 2c).

MD simulations have also shown that mixed surfactants are able to form a flatter monolayer at the water−vacuum interface than mono SOS surfactants. With the same surface coverage density as used in experimental ILE synthesis, the SOS monolayer at the water−vacuum interface exhibits a much higher roughness (Figure 3f) compared to the 9:1 SOS/OAM monolayer (Figure 3g). This phenomenon can be explained qualitatively by the electrostatic repulsion of SOS head groups, which in the case of the monosurfactant leads to increased surface area and interface crumbling. In the case of mixed surfactants, the electrostatic repulsion is screened by positively charged OAM head groups. Increasing OAM concentration further lowers the monolayer roughness to the level of 0.038 nm (Figure S10). The presence of Co^{2+} ions in the adjacent solution is also able to significantly reduce the roughness of the SOS monolayer (Figure 3h), although it is still rougher than the mix-charge monolayer (Figure 3i) at the same Co^{2+} concentration. Importantly, the roughness of the mix-charge monolayer is nearly constant as a function of Co^{2+} concentration (red and black curves in Figure 3j), whereas roughness of the monosurfactant increases with decreasing Co^{2+} concentration (the blue curve in Figure 3j). This means that as the nanosheets nucleate and Co^{2+} concentration decreases, the SOS monolayer may become gradually distorted, introducing defects into the nanosheets.

Experimentally, the mix-charge surfactant monolayer showed better ordering, as indicated by Fourier-transform infrared (FT-IR) spectra obtained from the mixed monolayer in the presence of Co^{2+} ions after transferring onto the Al_2O_3 substrates. The symmetric and antisymmetric stretching vibrations of the methylene groups were observed from mono SOS surfactant at 2854 and 2927 cm^{-1}, respectively (Figure 3k). However, these two peaks shifted to 2850 and 2918 cm^{-1}, respectively, when SOS was mixed with OAM at a 9:1 ratio. This shift to lower wavenumber indicated a more ordered structure of the alkyl tails in the surfactant monolayer.

The above analyses demonstrate that the stable, flat, and ordered monolayer enabled by mix-charge surfactants provided favorable conditions for the growth of monocrystalline 2D nanosheets with small and uniform thickness. Decreasing the SOS/OAM ratios further could lead to Co^{2+} concentration in the double layer being too low and, thus, suppress crystal formation. These synergistic effects might lead to the optimal mixing ratio of SOS/OAM = 9:1 for the growth of monocrystalline nanosheets. This hypothesis was further verified by using the mixed monolayer with various ratios to grow the same nanosheets. Monocrystalline triangular nanosheets can be synthesized with the mixed monolayer of SOS/OAM = 7:3 but with a lower yield, which was consistent to the prediction of lower Co^{2+} concentration within the double layer. When the net charge of the monolayer became positive (SOS/OAM < 5:5), no nanosheets could be formed (Figure S1).

The synthetic strategy of adapting mix-charge surfactants to the template crystal growth is generic and can be applied to synthesizing ultrathin 2D nanosheets from a myriad of multivalance metal oxides. As shown in Figure 4a, by using the same SOS/OAM mixture (9:1) at the water/air interface, it was possible to synthesize Bi_2O_3 nanosheets from the aqueous precursor solution of $Bi(NO_3)_3$ and HMTA. Square-shaped nanosheets were obtained as a result of the cubic phase of Bi_2O_3. They exhibited edge lengths of 1−2 μm and a thickness of 4.5 nm (Figure 4b). HRTEM and corresponding SAED pattern confirmed the monocrystallinity of the cubic Bi_2O_3 nanosheets (Figures 4c and S11). In addition, considering that both, carboxyl groups on oleic acid (OA) and amine groups on OAM, can react with permanganate to form MnO_2, mixing OA and OAM at a ratio of 9:1 was used to form 2D hexagonal MnO_2 nanosheets (Figure 4d) in acidic condition. The MnO_2 nanosheets exhibited a uniform hexagonal shape with sizes in the range of 1−2 μm and thicknesses of ∼2 nm (Figure 4e). They were monocrystalline, and the lattice was identified as the hexagonal birnessite (Figure 4f), well represented by the shape of the nanosheets.

In addition to pure-phase oxides, the mix-charge monolayer could also be used to introduce dopants to oxide nanosheets. Using the mixed nickel and zinc ion solution as a precursor under the SOS/OAM monolayer at a ratio of 7:3, monocrystalline Ni-doped ZnO nanosheets were successfully synthesized (Figure 4g). Continuous polycrystalline films were obtained for the SOS/OAM ratio of 9:1 and mono SOS (Figure S12). The preference for higher OAM ratio was possibly due to the requirement of higher interface flatness to interact with both types of cations simultaneously. All of the nanosheets exhibited a uniform thickness of 2 nm (Figure 4h). EDS element mapping confirmed the uniform distribution of Ni atoms within the triangular nanosheet (Figure S13). HRTEM and corresponding SAED pattern confirmed the monocrystalline structure of wurtzite ZnO (Figure 4i). The concentration of Ni in ZnO nanosheets can be readily tuned in the range of (0−10 atom %) by changing the ratio of the Ni^{2+} and Zn^{2+} in the precursor solution, while the morphology of the nanosheets still remained the same (Figure S14). While it is extremely challenging to uniformly dope nanosheets at the nanometer scale, the mix-charge surfactant opened a unique route toward doping 2D nanomaterials without influencing its morphology and monocrystallinity.

Beyond the all-solution-based synthesis conditions, the mix-charge surfactant ILE could be extended to a gas−liquid reaction system, with which thin films of crystalline Fe_3O_4 were synthesized (Figure S15). Here, to enhance the interaction between the Fe^{2+} and the monolayer, surfactants with hydroxyl group (1-octadecanol) were used.[35] The mixed monolayer of 1-octadecanol and OAM (1-octadecanol/OAM = 19:1) directed the growth of iron oxides films by reacting Fe^{2+} with NH_3 gas at the interface under room temperature. Due to the weak anionic properties of the 1-octadecanol, the mixed templates showed less stability than ionic mixtures of SOS and OAM, thus leading to irregular film formation (Figure 4j). Nevertheless, the thickness of the film was maintained around 2.5 nm (Figure 4k). HRTEM revealed the formation of monocrystalline domains of the Fe_3O_4 (Figure 4l).

■ CONCLUSIONS

In summary, by learning from biomineralization, we introduced the mix-charge surfactant template with positive and negative head groups to direct the ILE synthesis of large-area, single-crystalline nanosheets. This unique free-standing template enabled the formation of monocrystals by inducing concentrated metal ion regions in the electric double layer and aligning the orientation of the facets. Mixing charges yielded a stable, flatter, and a more ordered monolayer template with a nonuniform distribution of charges, which were able to tune the 2D crystal nucleation rate and promote the growth of

DOI: 10.1021/acs.chemmater.9b03307
Chem. Mater. 2019, 31, 9040−9048

monocrystalline domains. The mix-charge template showed great promises as a versatile synthesis paradigm for creating quasi-2D nanomaterials from a wide range of oxides, beyond van der Waals solids. This new 2D nanomaterial system will lead to the emerging of new or enhanced physical properties such as ferromagnetism (Figure S16), superconductivity, and single-photon emission.

EXPERIMENTAL SECTION

Synthesis of 2D Oxides. All nanosheets were prepared in a similar procedure at the water−air interface with different mixed surfactants. Take the synthesis of CoO nanosheets for example: 15 mL of the aqueous solution containing 5 mM cobalt nitrate and 25 mM hexamethylenetetramine (HMTA) was prepared in a 24 mL glass vial. Mixed surfactant solution of sodium oleylsulfate (SOS) and oleylamine (OAM) with a specific ratio (total concentration is 1.8 mM) was prepared in chloroform. Then, 8 μL of the mixed surfactants was dispersed on the solution surface. For achieving equilibrium of the monolayer and evaporation of the chloroform, 10 min was allowed. Subsequently, the vial was capped to form a closed reaction environment and placed in a 60 °C convection oven for 100 min to harvest monocrystalline nanosheets, which could be scooped using an arbitrary substrate for further characterization. To get the CoO nanosheets, the as-prepared $Co(OH)_2$ nanosheets were treated with O_2 plasma for 10 min. For nanosheets prepared with mono SOS, the procedure was exactly the same, except that 8 μL of the SOS chloroform solution was used.

Characterization. A Zeiss LEO 1530 Schottky-type field-emission scanning electron microscope was used to study the morphologies of the samples. A FEI TF30 transmission electron microscope operated at 300 kV was used to study the crystal structure of the samples. EDS in the scanning transmission electron microscope mode on a probe aberration-corrected FEI Titan at 200 kV was used for element mapping. The infrared spectra ware obtained from Nicolet Magna 860 FT-IR. Atomic force microscopy (AFM) tomography images were obtained using XE-70 Park Systems. The X-ray photoelectron spectroscopy (XPS) spectrum was obtained from a Thermo Scientific K-α XPS instrument with a 400 μm spot size, with the flood gun turned on during the measurements. Grazing incidence X-ray diffraction (GID) measurements were carried out on a beamline 15-ID-C (Chem-MatCARS) at the Advanced Photon Source (Argonne National Laboratories). The sample chamber was purged with helium to minimize air scattering. A Ge (111) steering crystal was used to direct monochromatic X-rays of energy 10.0 keV (λ = 1.24 Å) onto the air−water interface at appropriate incident angles. Diffracted X-rays were collected on a Pilatus 100K X-ray detector (Dectris). The superconducting quantum interference device quantum Design MPMS3 magnetometer was used for the measurements of the magnetization as a function of the applied magnetic field at 300 K. The magnetic property of CoO nanosheets was measured from a monolayer of densely distributed nanosheets supported on single-crystalline Al_2O_3 substrates. The magnetic field was applied parallel to the nanosheets.

Simulation Methods. All of the simulations are performed with GROMOS 54A7 force field as implemented in the GROMACS 5.1.2 software package. Many surfactant systems[11,36,37] have been successfully modeled with this force field. Force field parameters for SOS molecules are taken from ref 38 and are the same as in our previous study.[11] Interactions between ions of the same type are described using a combination of Lennard-Jones and Coulomb potentials with parameters the same as in refs 11, 38, 39. All of the intramolecular and intermolecular force field parameters (except for charge) for the head group of OAM molecules are taken directly from GROMOS 54A7 force field library and are listed in Tables S1 and S2, respectively. The charge of OAM, which is a parameter for Coulomb potentials included in the intermolecular force field, is taken from ref 40. Force field parameters for the carbon chain of OAM are the same as those of SOS's carbon chain and listed in ref 11. In Table S1, parameters K_b, K_θ, K_φ represent coefficients in different terms of the force field.[37] In particular, K_b enters the covalent bond bending term $K_b[r^2 - r_0^2]^2/4$, where r_0 is the equilibrium bond length. Molecular angle term is $K_\theta[\cos\theta - \cos\theta_0]^2/2$, where θ_0 is the equilibrium angle. K_φ is the coefficient in the dihedral angle term $K_\varphi[1 + \cos(\varphi_0)\cos(n\varphi)]$, where φ_0 is the phase shift, which is restricted to 0 or π, and n is the multiplicity of the torsional dihedral angle. Water is modeled using the SPC/E force field.[41] All intermolecular interactions are calculated using a combination of the Lennard-Jones potential (with parameters ε, σ) and Coulomb (electrostatic) potential. For Lennard-Jones interactions between different groups and different ions, we calculate parameters based on the geometric rule of mixture. Bond angles within the SOS molecules and OAM molecules were constrained using the LINCS algorithm, and bond angles in water molecules were constrained using the SETTLE. VMD 1.9.4 software, which was used for visualization.

ASSOCIATED CONTENT

Supporting Information

The Supporting Information is available free of charge on the ACS Publications website at DOI: 10.1021/acs.chemmater.9b03307.

Intramolecular parameters for amino group; intermolecular force field parameters; cobalt hydroxide nanosheets growth; EELS mapping; XPS of triangle nanosheets (PDF)

AUTHOR INFORMATION

Corresponding Author

*E-mail: xudong.wang@wisc.edu.

ORCID

Yizhan Wang: 0000-0003-0464-6610
Ziyi Zhang: 0000-0001-9102-8292
Jun Li: 0000-0002-7498-6736
Paul M. Voyles: 0000-0001-9438-4284
Izabela Szlufarska: 0000-0002-5895-8620
Xudong Wang: 0000-0002-9762-6792

Notes

The authors declare no competing financial interest.

ACKNOWLEDGMENTS

The authors thank Dr. Wei Bu for the help of GID data analysis and Dr. Alexander Kvit for the help of EELS characterization. This work was primarily supported by the Army Research Office (ARO) under grant W911NF-16-1-0198 and National Science Foundation DMR-1709025. I.S. and Y.S. gratefully acknowledge support from the Army Research Office grant ARO W911NF-17-1-0571. GID data was collected at NSF's Chem-MatCARS Sector 15 supported by the Divisions of Chemistry (CHE) and Materials Research (DMR), National Science Foundation, under grant number NSF/CHE-1346572. The use of the Advanced Photon Source, an Office of Science User Facility operated for the U.S. Department of Energy (DOE) Office of Science by Argonne National Laboratory, was supported by the U.S. DOE under Contract No. DE-AC02-06CH11357. TEM and STEM characterization (C.Z. and P.M.V.) were supported by the Department of Energy (DE-FG02-08ER46547) using facilities supported by the Wisconsin NSF MRSEC (DMR-1720415).

REFERENCES

(1) Zhang, F.; Zhang, H.; Krylyuk, S.; Milligan, C. A.; Zhu, Y.; Zemlyanov, D. Y.; Bendersky, L. A.; Burton, B. P.; Davydov, A. V.; Appenzeller, J. Electric-field induced structural transition in vertical

DOI: 10.1021/acs.chemmater.9b03307
Chem. Mater. 2019, 31, 9040−9048

$MoTe_2$- and $Mo_{1-x}W_xTe_2$-based resistive memories. *Nat. Mater.* **2019**, *18*, 55−61.
(2) Wu, J.; Chen, Y.; Wu, J.; Hippalgaonkar, K. Perspectives on Thermoelectricity in Layered and 2D Materials. *Adv. Electron. Mater.* **2018**, *4*, No. 1800248.
(3) Brar, V. W.; Koltonow, A. R.; Huang, J. New Discoveries and Opportunities from Two-Dimensional Materials. *ACS Photonics* **2017**, *4*, 407−411.
(4) Yu, Y.; Yu, Y.; Xu, C.; Cai, Y.-Q.; Su, L.; Zhang, Y.; Zhang, Y.-W.; Gundogdu, K.; Cao, L. Engineering Substrate Interactions for High Luminescence Efficiency of Transition-Metal Dichalcogenide Monolayers. *Adv. Funct. Mater.* **2016**, *26*, 4733−4739.
(5) Zavabeti, A.; Ou, J. Z.; Carey, B. J.; Syed, N.; Orrell-Trigg, R.; Mayes, E. L. H.; Xu, C.; Kavehei, O.; O'Mullane, A. P.; Kaner, R. B.; Kalantar-zadeh, K.; Daeneke, T. A Liquid Metal Reaction Environment for The Room-Temperature Synthesis of Atomically Thin Metal Oxides. *Science* **2017**, *358*, 332−335.
(6) Tan, C.; Zhang, H. Wet-chemical Synthesis and Applications of Non-Layer Structured Two-Dimensional Nanomaterials. *Nat. Commun.* **2015**, *6*, No. 7873.
(7) Yang, W.; Zhang, X.; Xie, Y. Advances and Challenges in Chemistry of Two-Dimensional Nanosheets. *Nano Today* **2016**, *11*, 793−816.
(8) Wang, F.; Wang, Z.; Shifa, T. A.; Wen, Y.; Wang, F.; Zhan, X.; Wang, Q.; Xu, K.; Huang, Y.; Yin, L.; Jiang, C.; He, J. Two-Dimensional Non-Layered Materials: Synthesis, Properties and Applications. *Adv. Funct. Mater.* **2017**, *27*, No. 1603254.
(9) Dou, Y.; Zhang, L.; Xu, X.; Sun, Z.; Liao, T.; Dou, S. X. Atomically thin non-layered nanomaterials for energy storage and conversion. *Chem. Soc. Rev.* **2017**, *46*, 7338−7373.
(10) Wang, F.; Seo, J.-H.; Luo, G.; Starr, M. B.; Li, Z.; Geng, D.; Yin, X.; Wang, S.; Fraser, D. G.; Morgan, D.; Ma, Z.; Wang, X. Nanometre-Thick Single-Crystalline Nanosheets Grown at The Water−Air Interface. *Nat. Commun.* **2016**, *7*, No. 10444.
(11) Yin, X.; Shi, Y.; Wei, Y.; Joo, Y.; Gopalan, P.; Szlufarska, I.; Wang, X. Unit Cell Level Thickness Control of Single-Crystalline Zinc Oxide Nanosheets Enabled by Electrical Double-Layer Confinement. *Langmuir* **2017**, *33*, 7708−7714.
(12) Sun, Z.; Liao, T.; Dou, Y.; Hwang, S. M.; Park, M.-S.; Jiang, L.; Kim, J. H.; Dou, S. X. Generalized self-assembly of scalable two-dimensional transition metal oxide nanosheets. *Nat. Commun.* **2014**, *5*, No. 3813.
(13) Zhuang, L.; Jia, Y.; He, T.; Du, A.; Yan, X.; Ge, L.; Zhu, Z.; Yao, X. Tuning oxygen vacancies in two-dimensional iron-cobalt oxide nanosheets through hydrogenation for enhanced oxygen evolution activity. *Nano Res.* **2018**, *11*, 3509−3518.
(14) Yin, X.; Chen, Q.; Tian, P.; Zhang, P.; Zhang, Z.; Voyles, P. M.; Wang, X. Ionic Layer Epitaxy of Nanometer-Thick Palladium Nanosheets with Enhanced Electrocatalytic Properties. *Chem. Mater.* **2018**, *30*, 3308−3314.
(15) Wang, F.; Yu, Y.; Yin, X.; Tian, P.; Wang, X. Wafer-Scale Synthesis of Ultrathin CoO Nanosheets with Enhanced Electrochemical Catalytic Properties. *J. Mater. Chem. A* **2017**, *5*, 9060−9066.
(16) Tian, P.; Yu, Y.; Yin, X.; Wang, X. A Wafer-Scale 1 nm $Ni(OH)_2$ Nanosheet with Superior Electrocatalytic Activity for the Oxygen Evolution Reaction. *Nanoscale* **2018**, *10*, 5054−5059.
(17) Fricke, M.; Volkmer, D. In*Biomineralization I: Crystallization and Self-Organization Process*; Naka, K., Ed.; Springer: Berlin, 2007.
(18) Evans, J. S. "Tuning in" to Mollusk Shell Nacre- and Prismatic-Associated Protein Terminal Sequences. Implications for Biomineralization and the Construction of High Performance Inorganic−Organic Composites. *Chem. Rev.* **2008**, *108*, 4455−4462.
(19) Harding, J. H.; Duffy, D. M.; Sushko, M. L.; Rodger, P. M.; Quigley, D.; Elliott, J. A. Computational Techniques at the Organic−Inorganic Interface in Biomineralization. *Chem. Rev.* **2008**, *108*, 4823−4854.
(20) Popescu, D. C.; Smulders, M. M. J.; Pichon, B. P.; Chebotareva, N.; Kwak, S.-Y.; van Asselen, O. L. J.; Sijbesma, R. P.; DiMasi, E.; Sommerdijk, N. A. J. M. Template Adaptability Is Key in the Oriented Crystallization of $CaCO_3$. *J. Am. Chem. Soc.* **2007**, *129*, 14058−14067.
(21) Shtukenberg, A. G.; Ward, M. D.; Kahr, B. Crystal Growth with Macromolecular Additives. *Chem. Rev.* **2017**, *117*, 14042−14090.
(22) Aizenberg, J.; Muller, D. A.; Grazul, J. L.; Hamann, D. R. Direct Fabrication of Large Micropatterned Single Crystals. *Science* **2003**, *299*, 1205−1208.
(23) Yao, H. B.; Ge, J.; Mao, L. B.; Yan, Y. X.; Yu, S. H. 25th Anniversary Article: Artificial Carbonate Nanocrystals and Layered Structural Nanocomposites Inspired by Nacre: Synthesis, Fabrication and Applications. *Adv. Mater.* **2014**, *26*, 163−188.
(24) Suzuki, M.; Saruwatari, K.; Kogure, T.; Yamamoto, Y.; Nishimura, T.; Kato, T.; Nagasawa, H. An Acidic Matrix Protein, Pif, Is a Key Macromolecule for Nacre Formation. *Science* **2009**, *325*, 1388.
(25) Metzler, R. A.; Evans, J. S.; Killian, C. E.; Zhou, D.; Churchill, T. H.; Appathurai, N. P.; Coppersmith, S. N.; Gilbert, P. U. P. A. Nacre Protein Fragment Templates Lamellar Aragonite Growth. *J. Am. Chem. Soc.* **2010**, *132*, 6329−6334.
(26) Bahn, S. Y.; Jo, B. H.; Choi, Y. S.; Cha, H. J. Control of Nacre Biomineralization by Pif80 in Pearl Oyster. *Sci. Adv.* **2017**, *3*, No. e1700765.
(27) Freeman, C. L.; Harding, J. H.; Quigley, D.; Rodger, P. M. Structural Control of Crystal Nuclei by an Eggshell Protein. *Angew. Chem., Int. Ed.* **2010**, *49*, 5135−5137.
(28) Collino, S.; Evans, J. S. Molecular Specifications of a Mineral Modulation Sequence Derived from the Aragonite-Promoting Protein n16. *Biomacromolecules* **2008**, *9*, 1909−1918.
(29) Collino, S.; Evans, J. S. Structural Features That Distinguish Kinetically Distinct Biomineralization Polypeptides. *Biomacromolecules* **2007**, *8*, 1686−1694.
(30) Hamm, L. M.; Giuffre, A. J.; Han, N.; Tao, J.; Wang, D.; De Yoreo, J. J.; Dove, P. M. Reconciling Disparate Views of Template-Directed Nucleation through Measurement of Calcite Nucleation Kinetics and Binding Energies. *Proc. Natl. Acad. Sci. U.S.A.* **2014**, *111*, 1304−1309.
(31) Wegst, U. G. K.; Bai, H.; Saiz, E.; Tomsia, A. P.; Ritchie, R. O. Bioinspired Structural Materials. *Nat. Mater.* **2014**, *14*, 23.
(32) Chuang, T. J.; Brundle, C. R.; Rice, D. W. Interpretation of the X-Ray Photoemission Spectra of Cobalt Oxides and Cobalt Oxide Surfaces. *Surf. Sci.* **1976**, *59*, 413−429.
(33) LaMer, V. K.; Dinegar, R. H. Theory, Production and Mechanism of Formation of Monodispersed Hydrosols. *J. Am. Chem. Soc.* **1950**, *72*, 4847−4854.
(34) Brown, M. A.; Bossa, G. V.; May, S. Emergence of a Stern Layer from the Incorporation of Hydration Interactions into the Gouy−Chapman Model of the Electrical Double Layer. *Langmuir* **2015**, *31*, 11477−11483.
(35) Lin, H.; Sakamoto, H.; Seo, W. S.; Kuwabara, K.; Koumoto, K. Crystal Growth of Lepidocrocite and Magnetite under Langmuir Monolayers. *J. Cryst. Growth* **1998**, *192*, 250−256.
(36) Schmid, N.; Eichenberger, A. P.; Choutko, A.; Riniker, S.; Winger, M.; Mark, A. E.; van Gunsteren, W. F. Definition and testing of the GROMOS force-field versions 54A7 and 54B7. *Eur. Biophys. J.* **2011**, *40*, 843−856.
(37) Oostenbrink, C.; Villa, A.; Mark, A. E.; Van Gunsteren, W. F. A biomolecular force field based on the free enthalpy of hydration and solvation: The GROMOS force-field parameter sets 53A5 and 53A6. *J. Comput. Chem.* **2004**, *25*, 1656−1676.
(38) Sammalkorpi, M.; Karttunen, M.; Haataja, M. Structural properties of ionic detergent aggregates: a large-scale molecular dynamics study of sodium dodecyl sulfate. *J. Phys. Chem. B* **2007**, *111*, 11722−11733.
(39) Li, P.; Roberts, B. P.; Chakravorty, D. K.; Merz, K. M. Rational design of particle mesh ewald compatible Lennard-Jones parameters for +2 metal cations in explicit solvent. *J. Chem. Theory Comput.* **2013**, *9*, 2733−2748.

DOI: 10.1021/acs.chemmater.9b03307
Chem. Mater. 2019, 31, 9040−9048

(40) Wang, L.; Hu, Y.; Liu, J.; Sun, Y.; Sun, W. Flotation and adsorption of muscovite using mixed cationic−nonionic surfactants as collector. *Powder Technol.* **2015**, *276*, 26−33.
(41) Berendsen, H. J. C.; Grigera, J. R.; Straatsma, T. P. The missing term in effective pair potentials. *J. Phys. Chem. A* **1987**, *91*, 6269−6271.

DOI: 10.1021/acs.chemmater.9b03307
Chem. Mater. 2019, 31, 9040−9048